

16. Needleman, A., 1987. A Continuum Model for Void Nucleation by Inclusion Debonding, *Journal of Applied Mechanics*, 54: 525-531.
17. Tvergaard, V., 1990. Effect of Fibre Debonding in a Whisker-Reinforced Metal, *Materials Science & Engineering A: Structural Materials: Properties, Microstructure, and Processing*, A125(2): 203-213.
18. Tvergaard, V. and J. W. Hutchinson, 1993. The Influence of Plasticity on Mixed Mode Interface Toughness, *Journal of the Mechanics and Physics of Solids*, 44: 1119-1135.
19. Allen, D. H., R. H. Jones and J. G. Boyd, 1994. Micromechanical Analysis of a Continuous Fiber Metal Matrix Composite Including the Effects of Matrix Viscoplasticity and Evolving Damage, *Journal of the Mechanics and Physics of Solids*, 42(3): 505-529.
20. Allen, D. H., D. C. Lo and M. A. Zocher, 1997. Modelling of Damage Evolution in Laminated Viscoelastic Composites, *International Journal of Damage Mechanics*, 6: 5-22.
21. Yang, B. and K. Ravi-Chandar, 1996. On the Role of the Process Zone in Dynamic Fracture, *Journal of the Mechanics and Physics of Solids*, 45(4): 535-563.
22. Costanzo, F. and D. H. Allen, 1994. A Continuum Mechanics Approach to Some Problems in Subcritical Crack Propagation, *International Journal of Fracture*, 63: 27-57.
23. Costanzo, F., J. G. Boyd and D. H. Allen, 1996. Micromechanics and Homogenization of Inelastic Composite Materials with Growing Cracks, *Journal of the Mechanics and Physics of Solids*, 44(3): 333-370.
24. Yoon, C. and D. H. Allen, 1998. Damage Dependent Constitutive Behavior and Energy Release Rate for a Cohesive Zone in a Thermoviscoelastic Solid, to appear in the *International Journal of Fracture*.
25. Zocher, M. A., D. H. Allen and S. E. Groves, 1997. A Three Dimensional Finite Element Formulation for Thermoviscoelastic Orthotropic Media, *International Journal for Numerical Methods in Engineering*, 40: 2267-2288.

Experimental Investigation of Beam-Column Behavior of Pultruded Structural Shapes

EVER J. BARBERO* AND MALEK TURK
Mechanical and Aerospace Engineering
West Virginia University
Morgantown, WV 26506-6106

ABSTRACT: The behavior of pultruded structural shapes under combined axial load and end moment is investigated experimentally. A combination of standard displacement transducers and full-field shadow moiré is used to record in real time all the deformation modes of the beam-column. A data reduction technique is proposed for interpretation of the full-field deformation data. Observations and quantitative data are presented regarding buckling initiation and collapse of five types of fiber-reinforced composite beam-columns.

INTRODUCTION

A FIBER REINFORCED plastic (FRP) is a composite material made of polymer resin reinforced with carbon, glass, or other fibers. Composite structural shapes, such as I-beams, are produced by pultrusion with geometry and material properties fixed by the manufacturer. A broad selection of such shapes is available for civil engineering construction [1-3]. Some advantages of composite materials are their high strength to weight ratio, resistance to environmental deterioration and their lack of interference with electromagnetic radiation. FRP columns and beams are being used in a variety of structures, such as buildings, salt storage sheds, bridge superstructures, etc. However, widespread application in construction is being hampered by lack of design information and methods. Structural engineering design does not involve changes in the material or the geometry of the cross-section but selection of the most appropriate shape from those available. Thus, the designer relies on information about the structural behavior of the member under the expected loads.

*Author to whom correspondence should be addressed.

Design equations for columns without bending and beams without axial load are available in the literature [4–9]. In many applications, columns are subjected to axial and bending loads simultaneously; in which case the member is called a beam-column (Figure 1). Bending moments on beam-columns may be caused by transverse loading acting over the member's span, from loading in adjacent members in frames, or by eccentricity of reactions and applied forces in frames. The scope of this paper is limited to the case of eccentricity producing bending with respect to the minor axis. Furthermore, no twisting occurs because the structural shapes considered are symmetric with respect to the major axis [10,11].

Since composite columns are thin-walled, buckling is a major consideration. Two types of column failure (buckling) are well known: local (flange) and global (Euler) column buckling. Local buckling occurs in short columns that are long enough not to fail due to crushing. For pultruded wide-flange (WF) sections (Figure 1), the column will compress axially until flanges develop wave like deformations along the length [5,12,13]. The flange deformations can be large, often greater than the thickness of the flanges. Therefore the local buckling load can be used as a failure criteria for short columns.

The short column buckling loads P_L reported in Table 1 were determined from short column tests as described by Tomblin and Barbero [13]. The values can be predicted also using analytical or numerical techniques [14–18]. The load P_L is independent of the length of the column as long as the column is short and wave modulation effect is not present [19].

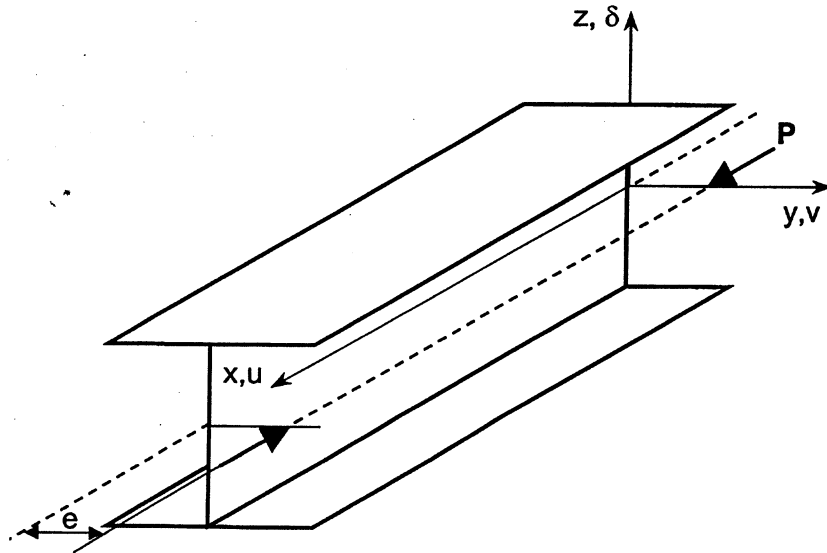


Figure 1. Geometry and coordinate system.

Table 1. Geometry and properties of the structural shapes tested.

Type	Denomination	Width [mm]	Depth [mm]	Thickness [mm]	(EI) [kN · m ²]	PL [kN]	L* [m]
A	4 × 4 × 1/4	102	102	6.35	29.66	226.95	1.14
B	6 × 6 × 1/4	152	152	flange:6.35 web:7.14	89.56	169.99	2.28
C	6 × 6 × 3/8	152	152	9.53	148.98	493.95	1.73
D	8 × 8 × 3/8	203	203	9.53	380.51	369.35	3.19
E	8 × 4 × 3/8	203	152	9.53	49.94	640.80	0.88

The Euler (global) mode occurs in slender columns and involves a sudden lateral deflection once the critical load is reached. This lateral movement occurs without deformation of the cross-section. Therefore, the Euler buckling load can be used as a failure criteria for a slender column. The Euler buckling equation

$$P_E = \frac{(EI)}{(kL / \pi)^2} \quad (1)$$

accurately predicts the critical buckling load for slender columns in terms of the bending stiffness (EI), the column length L , and the end-restraint coefficient k . The reduction of buckling load due to shear deformation can be accounted for by dividing the result of Equation (1) by $1 + P_E/(GA)$, where (GA) is the shear stiffness of the section [9,20,21]. The reduction is small for most practical cases. In addition the shear stiffness (GA) is difficult to measure accurately and thus is not reported in product literature. It is customary in steel design to predict (GA) as the product of the material shear modulus times the area of the web, when bending occurs about the strong axis. However, for composite WF shapes bending about the weak axis (GA) is not predicted accurately in this way (see Example 8.7 in Reference [22]). The bending stiffness (EI) can be measured from a bending test [4] or back calculated from a slender-column tests using Equation (1). The later method was used in this project.

When the axial load is applied at the neutral axis, without eccentricity, the column failure load can be estimated as [8]

$$P_c = k_i P_L \quad (2)$$

where P_L is the short-column load. The resistance factor k_i due to interaction between the local buckling of the flanges and the global (Euler) buckling of the column is

$$k_i = k_\lambda - \sqrt{k_\lambda^2 - \frac{1}{c\lambda^2}} \quad (3)$$

where $k_\lambda = (1 + 1/\lambda^2)/(2c)$, is a coefficient introduced for convenience, c is the empirical interaction constant adjusted to fit the data, and λ is the composite slenderness defined as

$$\lambda = \frac{kL}{\pi} \sqrt{\frac{P_L}{EI}} \quad (4)$$

where k is the end-restraint coefficient (see Table 8.1 in Reference [22]).

Data from [8,9,21,23,24] are shown in Figure 2 along with a plot of Equations (2)–(4) when the mode-interaction constant is set to $c = 0.84$. The isolated local and Euler curves are recovered by setting $c = 1$. In Equations (2)–(4), the material properties are introduced through the bending stiffness (EI) and the short-column load P_L , which are a function of both the material properties and the geometry of the cross-section. Values of (EI) and P_L were taken from the respective references while constructing Figure 2. The data from various sources is compared in dimensionless form because the material properties of the columns differ among manufacturers even for the same cross-section geometry.

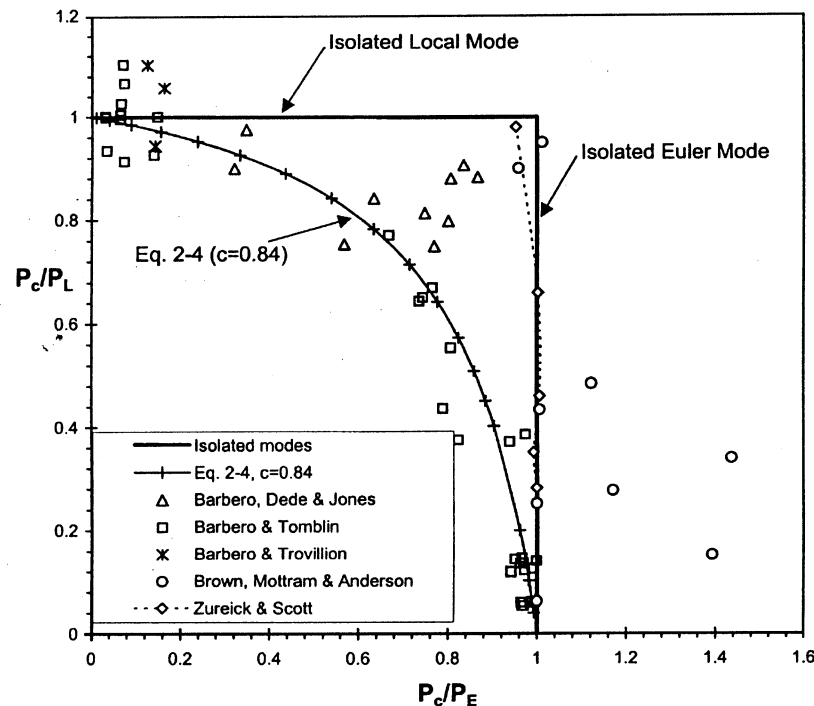


Figure 2. Failure load of columns subjected to axial load without eccentricity.

When the axial load is applied with eccentricity e with respect to the neutral axis of the column, an end-moment $M_0 = P \cdot e$ is generated. The end-moment produces lateral deformations from the onset of the loading and precipitates premature failure of the column. Therefore, the scope of this study is to investigate experimentally the behavior of pultruded columns when axially loaded with eccentricity. The deformation and failure are investigated using conventional test procedures coupled with the shadow moiré technique, capable of measuring full field, out-of-plane displacements. The contributions of the flange and lateral deformations to the overall behavior of the columns is readily observed, because the two deformations are characterized by distinct and measurable physical parameters.

The design of beam-columns with traditional materials is done using beam-column interaction diagrams that account for the reduction of column load capacity due to bending. For example, design of steel beam-columns is addressed by the AISC Manual of Steel Construction Allowable Stress Design, Section H1 Axial Compression and Bending and the AISC 1978 Specifications Section 1.6 [25]. Such diagrams do not exist for FRP structural shapes. Therefore, the objective of this paper is to provide the experimental data to support the development of design equations and accompanying diagrams. Such tools are necessary for the design of structures using FRP structural shapes.

EXPERIMENTAL SETUP

The beam-column tests were performed on a horizontal buckling frame about the weak axis of the specimens. The buckling frame, shown in Figure 3, was comprised of one fixed crosshead, one adjustable cross head, and one movable cross head. The adjustable crosshead adjusts in 305-mm increments, allowing for the testing of columns ranging in length from 1.2 to 6 m. Mounted to the inside of both the adjustable and the movable crosshead were two shoes with pin-and-needle bearings, which provide the pinned-pinned end conditions for the test.

All specimens were pultruded WF and I-beams provided by Creative Pultrusions, Inc [1]. The specimens were prepared using a band saw to cut the ends squarely with respect to the flange surface. It is critical to have the column ends cut flat and perpendicular to the column's axis, mainly with respect to the strong axis to prevent premature localized failure. This may occur because the pin-and-needle bearings provide only one degree of rotational freedom around the weak axis of the column. With respect to the weak axis, only a flat end is sought because the pinned shoe automatically adjusts to the end of the column. The axis of rotation of the pin-and-needle bearing is aligned with the flat end of the shoe on which the end of the column rests.

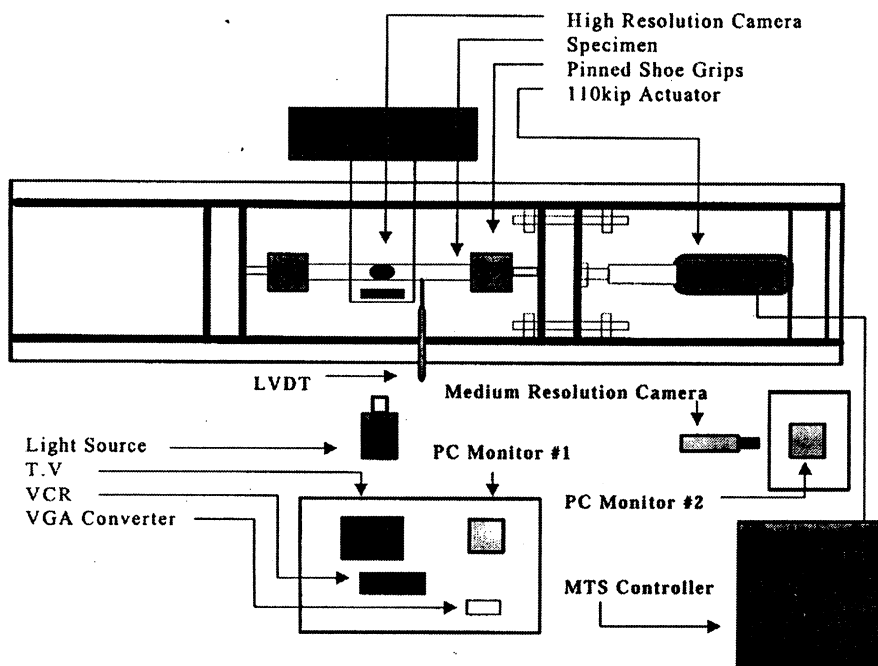


Figure 3. Experimental set-up used for beam-column buckling tests.

The columns were mounted in the frame in such a manner as to have one of the flange surfaces facing upwards. In this way, gravity acts on the strong axis, which is not tested, and there is no contribution to the Euler buckling mode due to gravity.

In order to apply load to the specimen, a MTS 500 kN hydraulic actuator with a ± 152 mm stroke was mounted between the fixed and movable crosshead. The MTS actuator was equipped with an internal (stroke) LVDT used to measure the stroke position of the actuator. The load was measured using a load cell mounted on the actuator in the line of loading. In order to measure the lateral movement, a ± 127 mm LVDT (lateral) PR 750-5000 LVDT was mounted to the side of the buckling frame and secured to the web of the sample using double-sided tape. Due to apparatus constraints, the lateral LVDT was not always placed directly at the center-point of the beam, but a few inches away. That variation however, is taken into account during data reduction assuming the Euler mode has a sinusoidal shape. In this way the corrected mid-span deflection is obtained as

$$\Delta = \Delta_{LVDT} / \sin(\pi X_{LVDT} / L) \quad (5)$$

in terms of the measured deflection Δ_{LVDT} , the length of the specimen L , and the actual position of the LVDT along the specimen measured from either end X_{LVDT} .

Data from the load cell, stroke LVDT, and lateral LVDT were conditioned using a MTS 458.10 Microconsole in order to achieve maximum sensitivity. The two displacement measurements (stroke and lateral) were conditioned using two MTS 458.14 conditioners, while the load was conditioned using one MTS 458.12 conditioner. The conditioned data were then passed to the data acquisition software using a Metrabyte DAS 16 data acquisition card. These data were recorded and displayed using Labtech Notebook Pro ver. 8.0 [26], installed on a 486/33 PC. Time, load, stroke, and lateral displacements were recorded in data files. The tests were performed using displacement control, specifying a stroke rate of 2.5 mm using a MTS 418.91 Microprofiler. At failure, the test was stopped and the actuator was returned to its initial position.

SHADOW MOIRÉ

The deformation of a beam-column not only contains lateral displacement, but also flange deformations that need to be recorded. Shadow moiré is an optical technique that can be used to measure out-of-plane displacement [27]. This method provides only a scalar quantity to represent the out-of-plane displacements. However, this technique is very powerful in that full-field deformations can be obtained in real time. Since this is a non-contact technique, the development of the buckling mode is unaffected by the instrumentation. The field deformations are recorded using a video acquisition system.

Creating the fringe field is accomplished by shining a light source at a 45° angle through a grating of desired frequency, producing a shadow or virtual grating on the surface of the specimen. When the physical and shadow gratings are parallel there are no fringes. Once the specimen experiences out-of-plane deformations, the shadow grating interferes with the physical grating, creating fringes when viewed normal to the original grating (Figure 4).

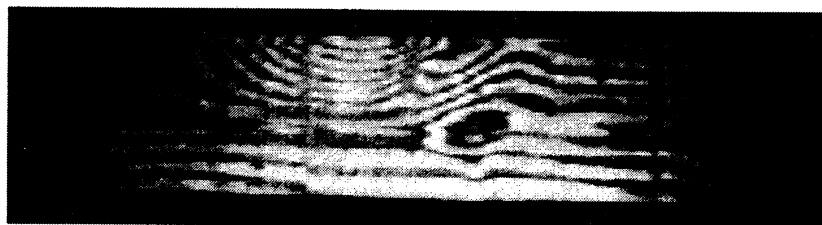
The amount of out-of-plane deformation that a specimen experience can be related by the number of fringes N_f , the pitch p of the grating, and the angle α between the light source and the normal to the grating

$$w = \frac{pN_f}{\tan \alpha} \quad (6)$$

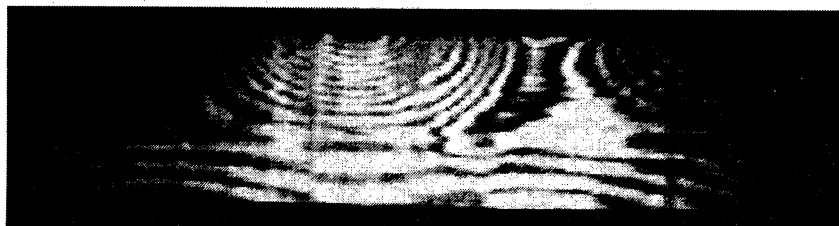
A grating of frequency 2.56 line/mm was used [28] and butt-jointed to create a viewing area 1300×250 mm. This was done in order to achieve an optimal dimension for viewing the deformation field as the sample also deforms laterally. Due to availability restrictions, a frequency grating of 2.16 line/mm was used for beams shorter than 1.575 m, and placed between two 900×250 mm glass plates. The



$P = 53.4 \text{ kN}$



$P = 164.6 \text{ kN}$



$P = 178.0 \text{ kN}$

Figure 4. Moiré fringes showing the progression of flange deformations on sample D4.

three gratings were mounted on plate glass using silicone spray. The silicone minimized air bubbles between the gratings and glass. Silicone proved to be a good choice in that it did not evaporate and did not deteriorate the gratings. The mounted glass was then suspended approximately 12.7 to 25.4 mm above the top flange surface of the specimen. The top flange surface was painted with flat white spray paint in order to enhance contrast. Choosing the top flange surface was a matter of visually inspecting both flange surfaces and picking the surface with the least amount of initial imperfections. The mounting frame used to suspend the grating enables free lateral adjustments from edge to edge of the frame and independent vertical adjustments at the four corners in order to zero the initial fringe field. Due to the initial imperfections of the columns and the high resolution of the technique, it was impossible to completely zero the initial field. Instead, the initial fringe pattern gives a contour plot of the initial imperfect shape of the flange.

VIDEO ACQUISITION

When a structural shape buckles, flange deformations occur. Tomblin and Barbero [13] measured and manually recorded flange deformations for locally buckled columns using four dial gauges positioned along a column's length. Using the recorded load and localized flange displacements, the local buckling load could be determined using Southwell's method [29]. A full-field optical recording method was developed in this project to capture flange deformation at every point, in real-time.

Video acquisition was used to record simultaneously the moiré image and the digital values of stroke, load, and lateral displacements. The video acquisition software Optimas can overlay two images obtained using two CCD cameras. The composite image is then sent to a video-recording device. The video acquisition system is PC based and consists of a MX-2MB monochrome frame grabber video card, video acquisition software [30] customized to overlay two separate video sources, one medium resolution CCIR camera, and one high resolution CCIR camera.

The high resolution CCIR camera (COHU 4990) fitted with a 12 mm lens (f1.2-16), was used to view the test sample. The medium resolution camera (COHU 4913) fitted with a 6 to 1 lens was used to view the data acquisition display from DAS computer (Data Acquisition System computer). The video signal from the two cameras is fed to the video acquisition computer via a serial connector on the MX-2MB frame grabber card. This connection keeps the two video-signals separate even though both must share the same input port. The video images were then compiled into one image using a program in Optimas. The video output was sent to a SVHS VCR, which recorded the composite image. This composite image can later be captured from the SVHS VCR using the view acquisition software.

A large field of view is needed for beam-column testing because the column deflects laterally as a result of the applied end moment. To view the desired 1300 mm test section, a camera frame was built next to the buckling frame, suspending the high-resolution camera 2.9 m above the test specimen. The camera frame allows for lateral adjustments and vertical adjustments to center the camera above the specimen and obtain the desired field of view. Besides supporting the camera, the frame also provided a means of draping lengths of cloth in order to keep as much ambient light as possible from reaching the test sample, as this would degrade the contrast.

Camera focus and aperture adjustments were needed to occur at the onset of each test. For safety and convenience, two geared, reversible DC motors were mounted next to the camera lens; one for the aperture, the other for focus. Sprockets on the shafts of the motors turned belts that rested tightly around the camera lens. Enough force was transmitted from the belt to the lens in order to turn the lenses at approximately 3 rpm, yet, the belts were able to slip once the maximum lens rotation was reached. The motors were controlled using two, three posi-

tion spring switches connected to a 12 volt power supply. This control box allowed for remote operation of the motors, approximately 12 m from the test.

EXPERIMENTAL PROCEDURE

Twenty-four different WF pultruded I-beams were tested at different lengths. Twenty-two were tested with eccentricity ($e = 25.4$ mm); and two were tested without eccentricity. There was no need to perform many tests without eccentricity since such data is available in the literature [9, 12, 13, 21, 23, 24]. Five different kinds of columns were used for this project. They are called $4 \times 4 \times 1/4$, $6 \times 6 \times 3/6$, $8 \times 4 \times 3/8$, and $8 \times 8 \times 3/8$, with the dimensions and material properties shown in Table 1. The behavior was consistent in most of the specimens tested. The columns were simply supported at both ends. Axial, lateral, and flange deformations were recorded in addition to the load (Table 2).

Ten specimens were prepared from the available WFI-beams to various lengths, shown in Table 1. Each specimen was mounted into the grips and snugged into place by moving the actuator until a slight load was read. The grating was then sus-

Table 2. Experimental results.

Sample	λ	P_b/P_L	P_u/P_L	P_δ/P_L	$(P_u - P_\delta)/P_L$	100 v/L*
A1*	0.89	0.186	0.302	0.304	0.16%	2.07
A2*	0.89	0.209	0.329	0.328	-0.14%	1.57
A3	1.23	0.176	0.261	0.260	-0.08%	1.89
B1	0.66	0.338	0.450	0.450	0.00%	0.22
B2*	0.69	0.209	0.463	0.483	1.94%	0.20
B3	0.80	0.288	0.448	0.463	1.53%	0.65
B4	0.80	0.288	0.448	0.458	0.99%	0.56
B5	0.94	0.262	0.395	0.400	0.45%	0.19
B6	1.07	0.183	0.419	0.423	0.46%	1.01
C1	1.06	0.306	0.398	0.405	0.65%	1.10
C2	1.06	0.261	0.389	0.404	1.51%	1.91
C3*	1.10	0.261	0.360	0.355	-0.49%	1.77
C4*	1.10	0.081	0.315	0.383	6.77%	1.52
D1	0.86	0.301	0.566	0.585	1.88%	0.96
D2	0.98	0.181	0.483	0.521	3.80%	1.27
D3	0.98	0.120	0.439	0.457	1.89%	1.35
D4	1.05	0.361	0.524	0.521	-0.29%	1.47
D5	1.05	0.361	0.454	0.455	0.06%	1.26
E1	1.82	—	0.158	—	—	3.26
E2	1.82	—	0.166	—	—	4.34
E3	3.13	—	0.060	—	—	5.01
E4	3.82	—	0.054	—	—	10.86
D6 **	0.60	—	0.973	0.983	0.95%	0.00
D7 **	0.60	—	0.898	0.918	2.06%	0.00

*End failure.

**No eccentricity.

ended above the specimen using the mounting fixture. The laboratory's interior lights were extinguished in order to lessen the effects of ambient light on the moiré picture. The light source was switched on in order to begin observing the initial moiré fringe pattern.

The data and video acquisition were initialized as the test started. One camera captured the fringe pattern development of the specimen, and the other camera captured load, stroke LVDT, and lateral LVDT measurements. The two camera signals were sent to the video acquisition computer and recorded on SVHS tape as a composite image.

The test was run at a stroke rate of at 2.5 mm/min according to the program stored in the MTS 458.10 Microprofiler. This stroke-rate was slow enough to observe the growth of the fringe pattern, yet provided reasonable test duration for taping purposes.

Once a loading of approximately 4.5 kN was achieved, the test was held at that load as efforts were made to zero the initial fringe pattern and attach the lateral LVDT used to measure lateral displacements. Once a satisfactory initial fringe pattern was achieved, the test resumed and continued until ultimate column failure. After failure, the actuator was returned to its initial position and the frame was prepared for the next experiment. After the test was complete, the images were recaptured, frame by frame, from the VCR into the computer. The images were then used to count the number of fringes as the load increased. The number of fringes was converted into flange displacements δ using Equation (6).

EXPERIMENTAL OBSERVATIONS

In this section, both the moiré and conventional data are used to describe the buckling behavior of the beam columns. Twenty-two out of twenty-four columns tested showed significant development of buckling modes before failure. The only two columns to fail by material crushing did so after very large lateral deflection, which would be inadmissible in a practical application due to serviceability constraints (samples E1-E2, Table 2). In addition, the following observations were made:

1. All columns had surface imperfections that caused initial fringes to appear. When processing the data, these initial fringes are subtracted from the overall fringe orders obtained throughout the duration of the test. The columns settled as loading was initially applied. In order to obtain the initial fringe pattern, the test was held at approximately 4.5 kN, and the initial fringe pattern was zeroed as best as possible.
2. The compression-side of the column had more fringe patterns than the tension-side because of the bending moment applied. Along with the increased number of fringe patterns, a lower wavelength was observed on the compression side (Figure 4).
3. As expected, load eccentricity results in a nonlinear load-deflection plot, as shown in Figure 5. The maximum load that can be reached reduces signifi-

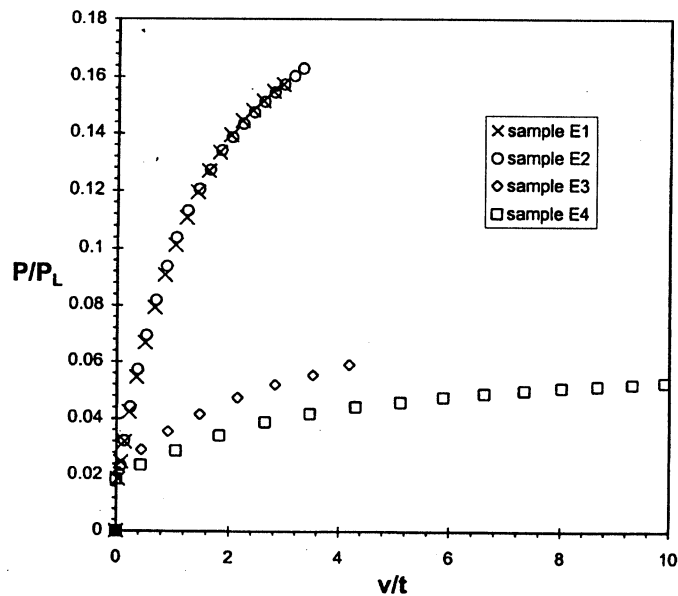


Figure 5. Load vs. lateral deflection plot.

cantly with respect to the column load without eccentricity. Lateral deflections v was measured at the midspan and normalized by the flange thickness t . The maximum flange deflection occurs at the edge of the flange.

SOUTHWELL'S METHOD

Previous research [13,23] showed that Southwell's data reduction technique [29] could be used to determine the critical buckling load for an imperfect column. Based on the assumption that the plot of $P - \delta$ acts as a rectangular hyperbola, with the P axis and the horizontal line $P = P_{cr}$ as asymptotes, P the measured load, and δ the measured deformation. If the horizontal asymptote can be determined, the critical load would be known. However, the asymptote is seldom reached during testing because of limitations of the equipment. Alternatively, it can be shown that the slope of the best-fit line for the plot of δ/P vs. δ is equivalent to the inverse of the critical load $1/P_{cr}$ (Figure 7). Imperfections in the column effect the y-intercept of the plot, but not the slope. Therefore, the correct critical load can be determined. The technique is used here to interpret the flange deformation data obtained from the moiré images. A single numerical value of critical load P_{δ} for each beam-column is then reported in Table 2 instead of reporting a plot such as Figure 6 for each sample.

For each column tested the $\delta/P - \delta$ plots were made for the moiré data. A linear regression was performed on the transformed data in order to obtain the equation

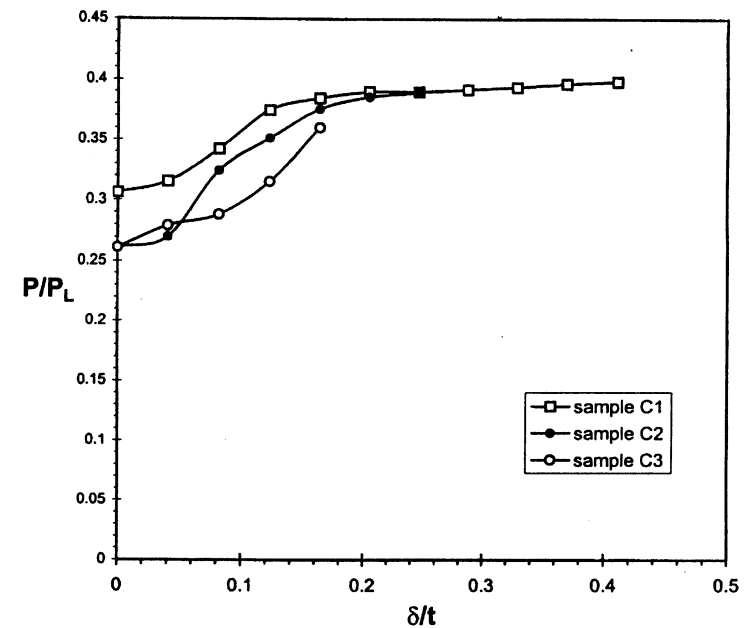


Figure 6. Load vs. flange deflection plot.

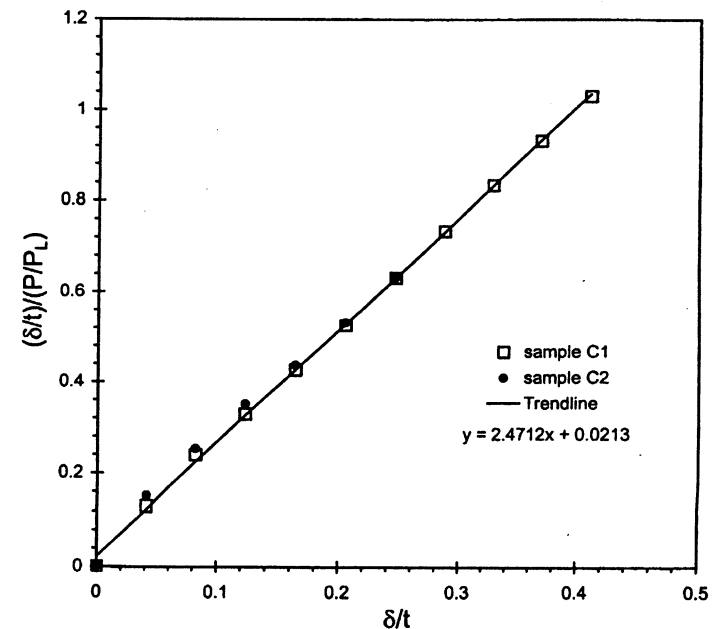


Figure 7. Southwell's plot of flange deflection.

for the best fit of the data. The results are presented in Table 2. The ultimate experimental load P_U , the bifurcation load P_b , and the critical buckling load determined from the moiré measurements P_δ , were normalized by the short-column load P_L . The bifurcation load was recorded as the last value of load for which no fringes were observed. In addition, the lateral deflection v at a load P_U is reported. The values are normalized with the length L^* at which the Euler and local buckling loads coincide ($\lambda = 1$) to provide for a meaningful interpretation of the magnitude of lateral deflection when such a variety of cross-sections are considered.

FINAL REMARKS

Based on the observations made, it was concluded that the main factors controlling failure of beam-columns are the eccentricity e , the column length, the material properties, and the geometry of the cross-section. All columns failed due to flange buckling as long as the bearing strength of the material at the ends of the sample was high enough to support the load (Figure 8). When flange buckling was precluded because the column was too slender, only lateral (global) deformations were observed (samples E1–E4). In these cases the material remained undamaged. The load deflection plots in Figure 5 could be retraced any number of times. Eventually, the crushing strength of the material was reached on the compression side and the column failed (Figure 9). However, from a design point of view, this situa-

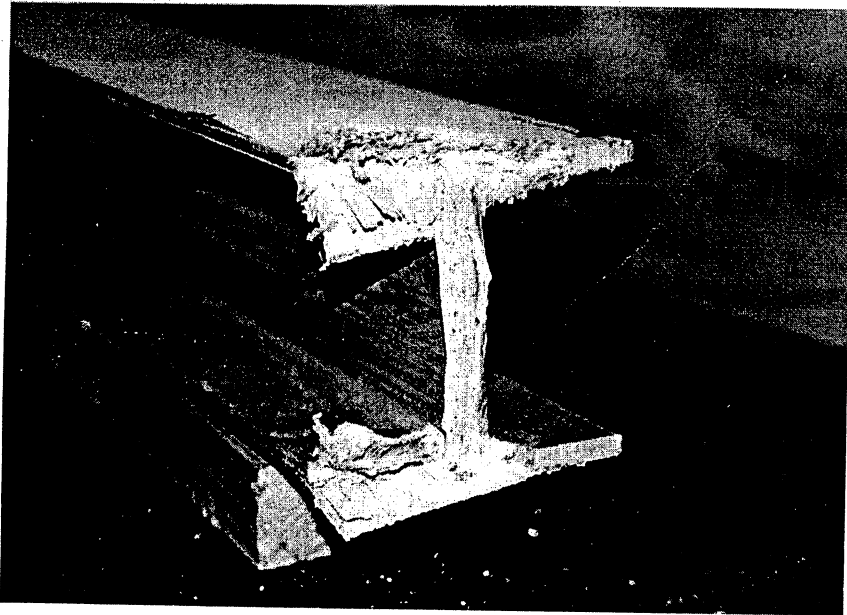


Figure 8. End failure of sample A2.

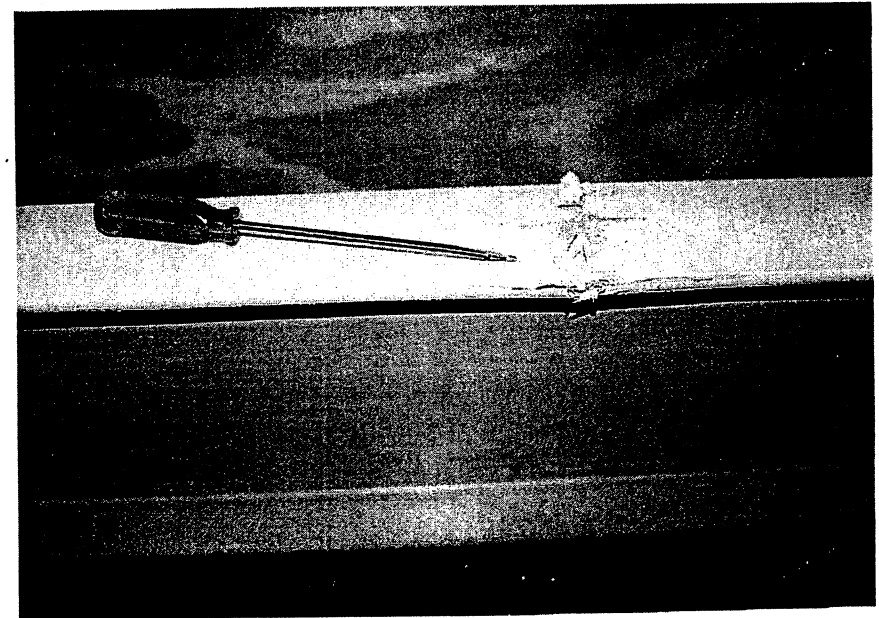


Figure 9. Compression failure of sample E2 while undergoing bending with respect to the weak axis.

tion would seldom be reached because serviceability constraints on the lateral deflection would be reached at a much lower load.

CONCLUSIONS

An experimental procedure was developed for obtaining relevant design information for pultruded structural shapes subject to end-loads with eccentricity. The information obtained includes the incipient buckling load, the critical load, and lateral as well flange deformation at failure. This was possible by using the shadow moiré technique and a data reduction technique demonstrated in this paper. The shadow moiré technique provides accurate flange deformation data, which in turn yields accurate prediction of the critical load where it is interpreted using Swallow's data reduction method. The information reported here for five different structural shapes can be used directly for structural design using those shapes or could be used to validate analytical or numerical predictions of the behavior of such shapes.

ACKNOWLEDGMENTS

The West Virginia Division of Highways sponsored this project under contract

RP #131. The financial support and the technical contribution of the project monitor, L. Galagedera, are appreciated.

REFERENCES

1. PULTEX Design Guide, Creative Pultrusions, Alum Bank, PA, 1989.
2. Strongwell Design Manual, Strongwell, Bristol, VA, 1994.
3. Bedford RP Design Guide, Bedford Reinforced Plastics, Inc., Bedford, PA, 1993.
4. Bank, L. C., Flexural and Shear Moduli of Full-Section Fiber Reinforced Plastic (FRP) Pultruded Beams, *Journal of Testing and Evaluation*, 17(1), 40–45, 1989.
5. Bank, L. C., and Yin, J., Buckling of Orthotropic Plates with Free and Rotationally Restrained Unloaded Edges, *Thin-Walled Structures*, 24, 83–96, 1996.
6. Bank, L. C., Nadipelli, M., and Gentry, T. R., Local Buckling and Failure of Pultruded Fiber Reinforced Plastic Beams, *J. Engineering Materials Technology*, 116, 233–237, 1994.
7. Bank, L. C., Yin, J., and Nadipelli, M., Local Buckling of Pultruded Beams—Nonlinearity, Anisotropy and Inhomogeneity, *Construction and Building Materials*, 9(6), 325–331, 1995.
8. Barbero, E. J. and J. Tomblin, A Phenomenological Design Equation for FRP Columns with Interaction Between Local and Global Buckling, *Thin-Walled Structures*, 18, 117–131, 1994.
9. Zureick, A. and D. Scott, Short-Term Behavior and Design of Fiber Reinforced Polymeric Slender Members under Axial Compression, *ASCE/Journal of Composites for Construction*, 14, 140–149, 1997.
10. Galambos, T. V., Guide to Stability Design Criteria for Metal Structures, Column Research Council, 4th Ed., John Wiley, New York, 1988.
11. Massa, J. C. and Barbero, E. J., A Strength of Materials Formulation for Thin Walled Composite Beams with Torsion, *Journal of Composite Materials*, 32(17), 1560–1594, 1998.
12. Pecce, M., Lazzaro, F., and Cosenza, E., Local Buckling of FRP Profiles: Experimental Results and Numerical Analyses, *European Conference on Composite Materials ECCM-8*, 331–338, Napoli, Italy, 1998.
13. Tomblin, J. and E. J. Barbero, Local Buckling Experiments on FRP Columns, *Thin-Walled Structures*, 18, 97–116, 1994.
14. Banks, W. M., and Rhodes, J., The Instability of Composite Sections, *2nd Int. Conf. on Composite Structures*, Paisley, UK, Elsevier, 442–452, 1983.
15. Barbero, E. J., and Raftoyiannis, I. Buckling Analysis of Pultruded Composite Columns, *Impact and Buckling of Structures*, ed. D. Hui, ASME AD—Vol. 20, AMD, Vol. 114, 47–52, 1990.
16. Dayalos, J. F. and Qiao, P., Engineering Design Analysis Equations for Local Buckling of FRP Structural Shapes, *2nd Int. Conf. on Composites in Infrastructure*, 2, 248–260, Tucson, AZ, 1998.
17. Morey, T. A., Johnson, E., and Shield, C. K. A Simple Beam Theory for the Buckling of Symmetric Composite Beams Including Interaction of In-Plane Stresses, *Composite Science and Technology*, 58, 1321–1333, 1998.
18. Yuan, R. L., Hashen, Z., Green, A. and Bisarnsin, T., Fiber Reinforced Plastic Composite Columns, *Adv. Composite Materials in Civil Eng. Structures*, 205–211, ed., S. L. Iyer, ASCE, Las Vegas, NV, 31 Jan.–1Feb., 1991.
19. Raftoyiannis, I., Godoy, L. A. and Barbero, E. J., Buckling Mode Interaction in Composite Plate Assemblies, *Applied Mechanics Reviews*, 52–60, 48 (11, Part 2), November, 1995.
20. Gaylord, E. H. and Gaylord, L. N., *Design of Steel Structures*, McGraw Hill, 2nd. Ed., 1972.
21. Brown, N. D., J. T. Mottram, and D. Anderson, The Behavior of Columns for the Design of Pultruded Frames: Tests on Isolated Centrally Loaded Columns, *2nd Int. Conf. on Composites in Infrastructure*, 2, 248–260, Tucson, AZ, 1998.
22. Barbero, E. J., *Introduction to Composite Materials Design*, Taylor and Francis, Philadelphia, PA, 1999.
23. Barbero, E. and J. Trovillion, Prediction and Measurement of the Post-Critical Behavior of Fiber-Reinforced Composite Columns, special issue on Civil Infrastructural Applications of Composite Materials, 58(8), 1335–1341, 1998.
24. Barbero, E. J., Dede, E., and Jones, S., Experimental Validation of Buckling Mode Interaction in Intermediate Length Composite Columns, *I. J. Solid Structures*, to appear, 1999.
25. American Institute of Steel Construction (AISC) Manual of Steel Construction Allowable Stress Design (ASD) Design Manual, Ninth Edition, 1989, American Institute of Steel Construction, Chicago, IL.
26. Labtech Notebook, Laboratory Technologies Co., Wilmington, MA, 1994.
27. Schwarz, R. C., Determination of Out-of-Plane Displacements and the Initiation of Buckling in Composite Structural Elements, *Experimental Techniques*, 23–28, 1988.
28. By Chrome, Columbus, OH, 1975.
29. Southwell, R. V., On the Analysis of Experimental Observations in Problems of Elastic Stability, *Proc. Royal Soc. London (A)*, 135, 601–616, 1932.
30. Optimas, BioScan Inc., Edmonds, WA, 1993.